Received: 7 October 2019 | Revised: 17 October 2019 | Accepted: 18 October 2019

DOI: 10.1002/mdp2.111

SPECIAL ISSUE ARTICLE

WILEY

Effect of wall thinning on deformation and failure of copper-nickel alloy elbows subjected to low cycle fatigue

Muhammad Faiz Harun[1] | **Roslina Mohammad**[1] | **Andrei Kotousov**[2]

[1]UTM Razak Faculty of Technology and Informatics, Universiti Teknologi Malaysia, Kuala Lumpur, Malaysia

[2]School of Mechanical Engineering, The University of Adelaide, Adelaide, South Australia, Australia

Correspondence
Dr Roslina Mohammad, Razak Faculty of Technology and Informatics, Universiti Teknologi Malaysia, Razak Tower, Jalan Sultan Yahya Petra, 54100 Kuala Lumpur, Malaysia.
Email: mroslina.kl@utm.my; puteriadelaide@yahoo.com

Funding information
Razak Faculty of Technology and Informatics and Universiti Teknologi Malaysia (UTM), Grant/Award Number: R. K130000.7840.4F852 Q. K130000.2540.19H15 Q. K130000.2656.16J42 Q. K130000.2540.19H15; Ministry of Higher Education, Malaysia, Grant/Award Number: MyBrain15 MyPhD

Abstract

Various industrial standards and safety regulations specify the minim number of cycles, which pressure equipment must tolerate during a single seismic event. The compliance with these standards and regulations is necessary in order to ensure safety and strength of critical structural components, eg, pressure pipe system of the primary coolant loop of nuclear reactors or condensed water supply of large hospitals or other large facilities. However, the strength can degrade with time due to flow accelerated corrosion causing wall thinning. Pipe bends are particularly susceptible to the localised corrosion, and, therefore, these structural elements need a special consideration. The current paper studies the effect of localised corrosion on low cycle fatigue behaviour of a copper-nickel elbows using experiment and finite element method (FEM). The outcomes of the study demonstrate a quite low reduction of low cycle fatigue life even at severe local wall thinning at different locations.

1 | INTRODUCTION

Pipe bends and elbows are common structural elements and often represent the weakest link[1] in pressure piping during extreme loading such as earthquakes.[2,3] Therefore, their performance and behaviour during seismic events are critical from the structural integrity point of view. Various industrial standards, such as ASME and the Japanese JEAC, specify the minimum number of cycles, which pressure equipment must tolerate during a single seismic event.[4-7] However, bends and elbows over time are subjected to the flow accelerated corrosion leading to the localised wall thinning.[8-10] Therefore, it is important to understand the effect of these structural defects on the strength in order to maintain the safety and integrity of hazardous structures. This problem was also emphasised during investigations of the integrity and residual strength of piping containing wall thinning defects after recent powerful earthquakes in Japan.[11]

In the case of extreme event (eg, earthquake or shut down), the piping elements are subjected to high amplitude loading excursions, leading to material cycling in low cycle fatigue regime.[12,13] There were many analytical, numerical, and experimental studies in this area with the ultimate aim of developing a method for the evaluation of low fatigue strength of various piping elements with various wall thinning defects with and without internal pressure.[2,10,11,14-25] For steel elbows, the recent studies have demonstrated that when the elbows are subjected to high amplitude cyclic

loading, the cross-section geometry distorts and bulges progressively with number of cycles, while the failure mechanism is largely associated with the initiation and propagation fatigue cracks.[11,18]

The focus of the current study is the effect of the localised wall thinning on the low cycle fatigue resistance of elbows made of copper-nickel alloy. For this purpose, a series of full-scale tests has been conducted under displacement-controlled loading conditions. The experimental study has motivated the development of the 3D elastoplastic finite element model (FEM) to assist with the interpretation of the outcomes of experimental studies.

2 | DETAILS OF EXPERIMENTAL AND NUMERICAL STUDY

Pipe elbows (or 90° bends) were made of C70600 copper-nickel 90/10 alloy (90% copper and 10% nickel), which is a common material for piping equipment. The test specimens consisted of the pipe elbow and two straight pipe segments that joined together by welding. The welding was completed using tungsten inner gas (TIG) welding machine. The outer diameter and wall thickness were 108 and 2.5 mm, respectively. The ratio of straight pipe segment length to the pipe outer diameter was about 3.2, which was consistent with the previous studies.[15] Other main dimensions are provided in Figure 3.

The specimens were tested with configuration as shown in Figure 1A, at the room temperature utilising a universal testing machine INSTRON 5982. One end (the lower end) of the specimens was attached to the testing machine grip through a pin joint, and another end (the upper end) was subjected to cyclic displacement-controlled loading with the displacement range of ±20 mm. The specimens were equipped with strain gauges as illustrated in Figure 1B, which were attached to intrados, extrados, and the crown areas of the elbow. The collected strain data were used to validate the numerical model.

Flow-induced corrosion defects (wall thinning) of various severity were introduced by machining the inner pipe surfaces near the crown, intrados, and extrados areas, as illustrated in Figure 2. The severity of the local thinning is characterised by the different ratio of the machining depth to the wall thickness (t/h). The specimens with the following range of values were tested: 0.25, 0.5, and 0.75.

In this investigation, a total of nine specimens were prepared with wall thinning was created on the elbow using machining process. The machining process was done using CNC milling. Each specimen only has one wall thinning spot with specific depth ratio either at intrados, crown, or extrados. The test was done until failure happen. The failure was indicated by observing the appearing of crack using naked eyes.

In order to support experimental studies a 3D elastoplastic FEM was developed in order to investigate the stress and strain field in other than the strain gauge locations. The geometry of the model and the mesh, which was based on the hexahedral finite elements (FEs), are shown in Figure 3. A denser mesh was used in the middle of the specimen where the large gradients of stress and strain were expected. The mesh convergence tests were done, and the optimum configuration achieved with the total number of elements and number of nodes is 54 227 and 96 222, respectively.

The finite element analysis (FEA) in this study was performed using Ansys Workbench 18.1 using an APDL solver and model was prepared using Ansys SpaceClaim 18.1. The strain-life approach was used to estimate the low cyclic fatigue of the model. The material behaviour of this FEA was based on elastoplastic hardening solid with rate-independent category.[26]

In this study, the kinematic isotropic hardening model was used in order to simulate the material behaviour under cyclic loading. The constitutive equation was based on the linear elasticity, von Mises yield function, and associative plastic flow rule.

The material constants utilised in the numerical study are presented in Table 1.

where E is Young modulus and K' and n' are the cyclic hardening coefficient and exponent of the stabilised cyclic of the stress in the Ramberg-Osgood equation, which was utilised to model the inelastic response of the material and strain curve; ε is total strain range, ε_e is the elastic strain range, and ε_p is the plastic strain range. The data above obtained from curve fitting method on the experimental strain-life curves and cyclic stress-strain curve.

The failure is evaluated using the standard the Basquin-Coffin-Manson criterion,[27] which can be written as

$$\frac{\Delta\varepsilon}{2}=\frac{\Delta\varepsilon_e}{2}+\frac{\Delta\varepsilon_p}{2}=\frac{\sigma_f'}{E}(2N)^b+\varepsilon_f'(2N)^c. \quad (2)$$

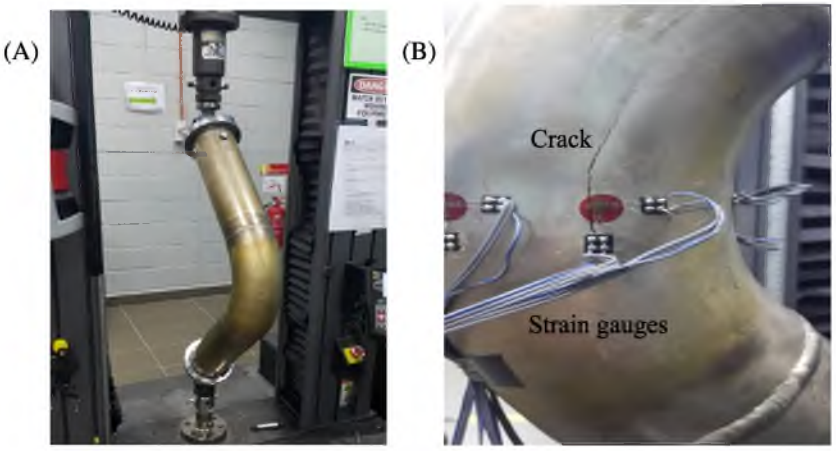

FIGURE 1 A, Elbow test specimen. B, Locations of strain gauges and failure (crack)

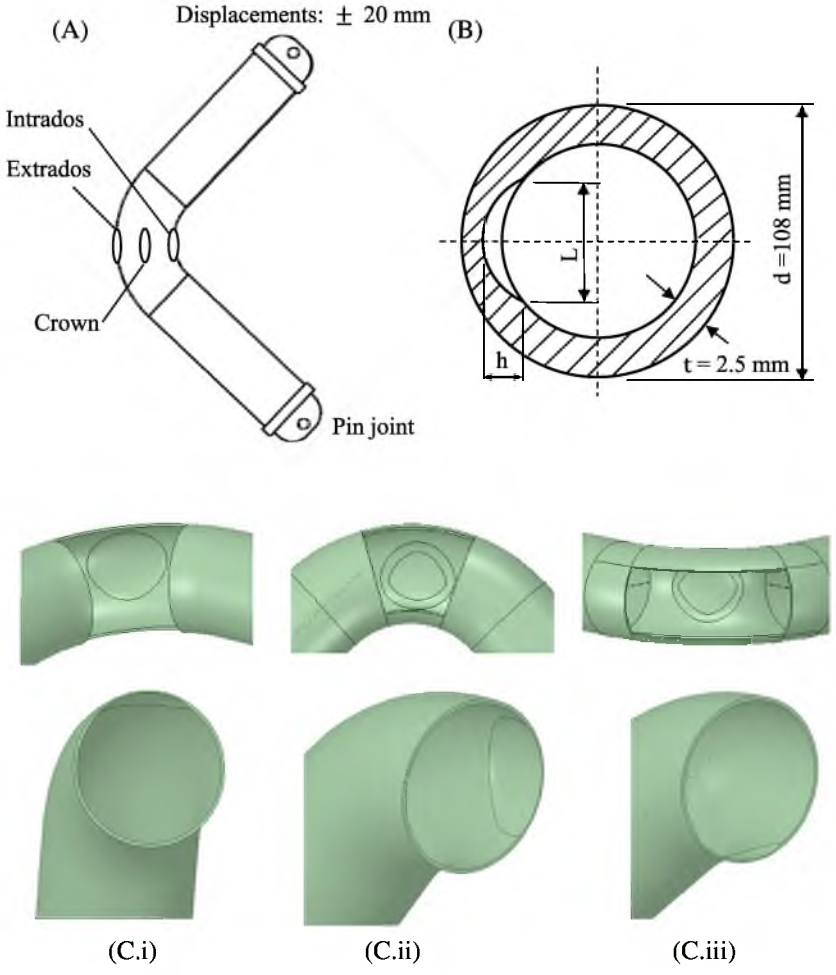

FIGURE 2 A, Test specimen and the areas of wall thinning; B, Cross sectional area and detect dimensions; and 3D elbow model with thin wall at (C.i) extrados, (C. ii) crown, and (C.iii) intrados

3 | OUTCOMES OF NUMERICAL AND EXPERIMENTAL STUDIES

The typical FE strain results are shown in Figure 4 indicating that the critical location is in the crown area on the inner wall, which agrees with the experimental findings, see Figure 1B and Table 2.

Figures 5 and 6 show the typical results of both FE (dotted lines) and experiment studies (solid lines) for the reaction force (Figure 5) and longitudinal strains at the crown location (Figure 6). A good agreement can be observed from these

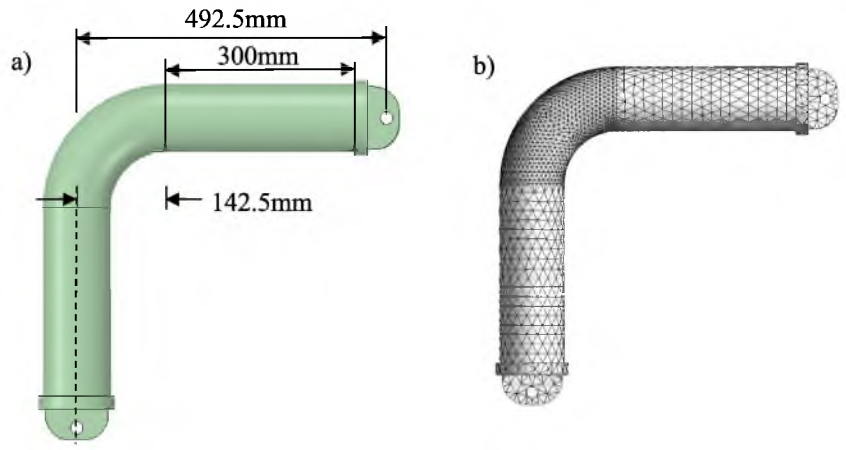

FIGURE 3 A, Main dimensions of the test specimen. B, Finite element (FE) mesh

TABLE 1 The values of the material constants

E, GPa	*K′*	*n′*	σ_f'	ε_f'	*b*	*c*
121.94	523	0.2172	6.9E+08	0.6	−0.13	−0.7

$$\frac{\Delta\varepsilon}{2}=\frac{\Delta\varepsilon_e}{2}+\frac{\Delta\varepsilon_p}{2}=\frac{\Delta\sigma}{2E}+\left(\frac{\Delta\sigma}{2K}\right)^{1/n'} \quad (1)$$

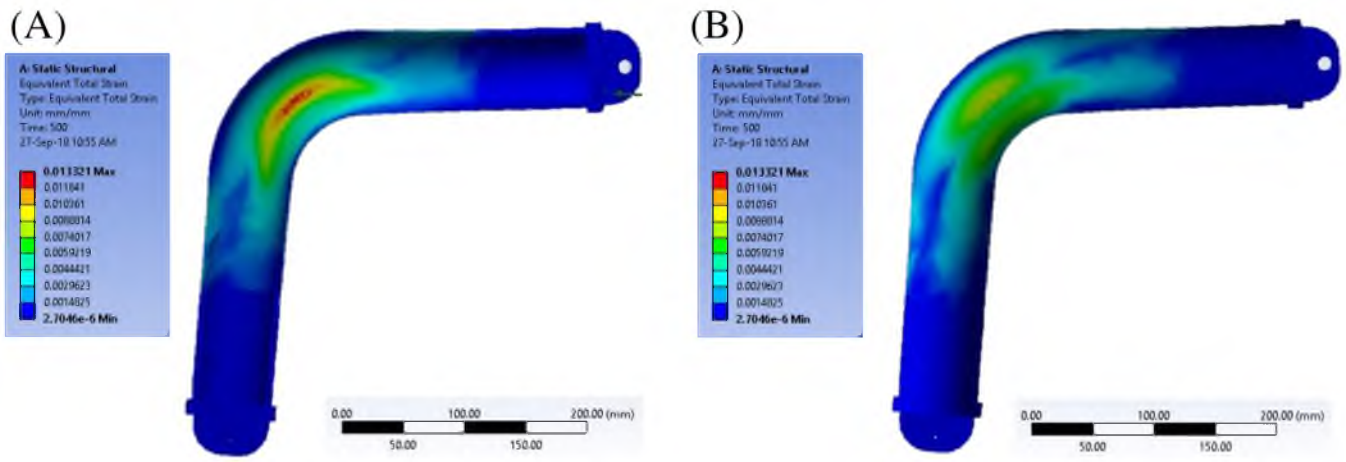

FIGURE 4 Equivalent plastic strains after 208 cycles. A, Inner wall view; B, outer wall

TABLE 2 Summary of experimental and FEM results

	Eroded Ratio (*h*/*t*)								
	Extrados			Crown			Intrados		
Life (N_f)	0.25	0.5	0.75	0.25	0.5	0.75	0.25	0.5	0.75
Experiment	193	187	179	184	172	166	201	198	194
FEM	195	190	175	181	169	161	203	196	189

Abbreviation: FEM, finite element method.

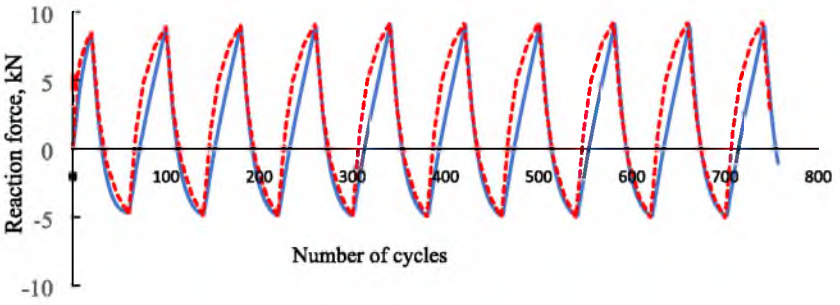

FIGURE 5 Reaction force during elbow cycling: Finite element (FE) results (dotted line) and experimental measurements (solid line)

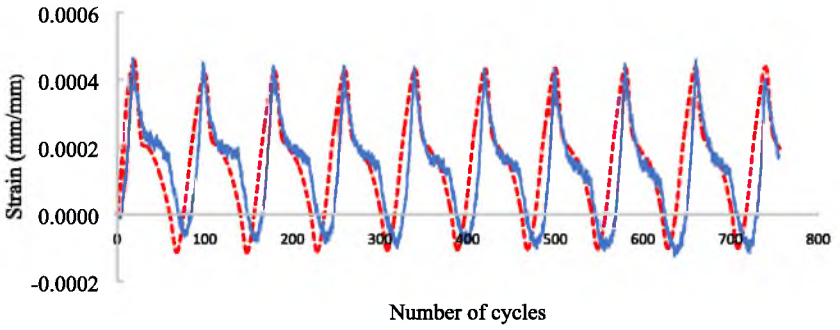

FIGURE 6 Comparison of finite element analysis (FEA) and experimental data strain gauge measurements

figures indicating that a careful FE analysis is capable to describe low cycle fatigue response. The change in slope of strain evolution shows the complexity strain at that location.

Table 2 presents the experimental and FEM data summarising the number of cycle to failure (crack initiation), N_f, for elbows with different wall thinning location: extrados, crown, and intrados, see Figure 2. The uses of the appropriate numerical model together with correct input data have effectively produced a reliable outcome which is nearly equal with actual results. The combination of isotropic and kinematic hardening rule model has tremendously come out with great results especially in terms of simulating the material plastic behaviours under cyclic loading.

The experimental results indicate that the location of the wall thinning (extrados, crown, and intrados; see Figure 2) does not significantly affect the low cycle fatigue life of copper-nickel alloy elbows. In the case of this investigation, it seems that the wall thinning at the crown location has the largest impact on low cycle fatigue strength. However, this impact is quite small, even for sever thinning $h/t = 0.75$) the reduction in the fatigue strength is only 10%, which is comparable with the scatter in experimental results.

4 | CONCLUSIONS

In this paper, the effect of localised corrosion (or wall thinning) on low cycle fatigue behaviour of a copper-nickel alloy elbows was investigated experimentally and using FEA. It was demonstrated that the actual deformations at the critical locations can be accurately predicted by FEM. Therefore, the further investigations can rely on the FE modelling with a limited number of full-scale tests.

The outcomes of the experimental studies demonstrated a quite low reduction of low cycle fatigue life of the elbows even at severe local wall thinning. The latter conclusion agrees well with the previous experimental studies for steel components.

ACKNOWLEDGEMENTS

The authors would like to express their greatest appreciation and utmost gratitude to the Ministry of Higher Education, Malaysia, for awarding the Fundamental Research Grant Scheme, MyBrain15 MyPhD, and Razak Faculty of Technology and Informatics and Universiti Teknologi Malaysia (UTM) for all the support towards making this study a success. FRGS UTM Vote No: R.K130000.7840.4F852, UTM Vote No: Q.K130000.2540.19H15, and UTM Vote No: Q.K130000.2656.16J42.

CONFLICT OF INTEREST

The authors confirm that there are no known conflicts of interest associated with this publication

AUTHOR CONTRIBUTIONS

M.F. Harun, R. Mohammad, and Andrei Kotousov contributed to the design and implementation of the research, to the analysis of the results, and to the writing of the manuscript.

ORCID

Roslina Mohammad https://orcid.org/0000-0003-3789-3706

REFERENCES

1. Chen, X. H., & Chen, X. (2013, November). Numerical simulations of pressurized elbow under reversed in-plane bending. In *Advanced Materials Research* (Vol. 785, pp. 16-19).
2. Li, X. H. (2012, January). Hoop membrane stress analysis of elbow-pipe under single internal pressure. In *Applied Mechanics and Materials* (Vol. 130, pp. 1785-1788).
3. Lu, X. Y., Li, X. G., Liu, J. M., Lu, X. L., Zhu, H. L., & Zhou, Y. (2015, January). Numerical simulation of flow fluid in elbow pipe based on FLUENT and the establishment of the pressure model. In *Applied Mechanics and Materials* (Vol. 713, pp. 39-42). Trans Tech Publications.
4. Hasegawa K, Miyazaki K, Nakamura I. Failure mode and failure strengths for wall thinning straight pipes and elbows subjected to seismic loading. *Journal of Pressure Vessel Technology*. 2008;130(1):011404-1-011404-8.
5. Nakamura I, Otani A, Shiratori M. Failure behavior of piping systems with wall thinning under seismic loading. *Journal of Pressure Vessel Technology*. 2004;126(1):85-90.
6. Ravikiran A, Dubey PN, Agrawal MK, Reddy GR, Singh RK, Vaze KK. Experimental and numerical studies of ratcheting in a pressurized piping system under seismic load. *Journal of Pressure Vessel Technology*. 2015;137(3):1-7.
7. Van KD, Moumni Z. Evaluation of fatigue-ratcheting damage of a pressurised elbow undergoing damage seismic inputs. *Nuclear Engineering and Design*. 2000;196(1):41-50.
8. Gao, B. J., Chen, X., Zhang, S. F., & Li, J. H. (2007, December). A proposed thickness distribution of elbow resisting ratcheting. In *Key Engineering Materials* (Vol. 353, pp. 377-380).
9. Firoozabad ES, Jeon BG, Choi HS, Kim NS. Failure criterion for steel pipe elbows under cyclic loading. *Engineering Failure Analysis*. 2016;66:515-525.
10. Kim JW, Na YS, Lee SH. Experimental evaluation of the bending load effect on the failure pressure of wall-thinned elbows. *Journal of Pressure Vessel Technology*. 2009;131(3):1-8.
11. Urabe Y, Takahashi K, Sato K, Ando K. Low cycle fatigue behavior and seismic assessment for pipe bend having local wall thinning-influence of internal pressure. *Journal of Pressure Vessel Technology*. 2013;135(4):1-5.
12. Takahashi K, Ando K, Matsuo K, Urabe Y. Estimation of low-cycle fatigue life of elbow pipes considering the multi-axial stress effect. *Journal of Pressure Vessel Technology*. 2014;136(4):1-8.
13. Takahashi K, Tsunoi S, Hara T, et al. Experimental study of low-cycle fatigue of pipe elbows with local wall thinning and life estimation using finite element analysis. *International Journal of Pressure Vessels and Piping*. 2010;87(5):211-219.
14. Takahashi K, Watanabe S, Ando K, et al. Low cycle fatigue behaviors of elbow pipe with local wall thinning. *Nuclear Engineering and Design*. 2009;239(12):2719-2727.
15. Urabe Y, Takahashi K, Abe H. Low cycle fatigue evaluation of pipe bends with local wall thinning considering multi-axial stress state. *Journal of Pressure Vessel Technology*. 2015;137(4):1-9.
16. Urabe Y, Takahashi K, Ando K. Low cycle fatigue behavior and seismic assessment for elbow pipe having local wall thinning. *Journal of Pressure Vessel Technology*. 2012;134(4):1-5.
17. Urabe Y, Takahashi K, Matsuo K, Sato K, Abe H. Theoretical study on low cycle fatigue strength of elbows with local wall thinning. *Nihon Kikai Gakkai Ronbunshu, A Hen/Transactions of the Japan Society of Mechanical Engineers, Part A*. 2013;79(804):1303-1316.
18. Varelis GE, Karamanos SA. Low-cycle fatigue of pressurized steel elbows under in-plane bending. *Journal of Pressure Vessel Technology*. 2015;137(1):1-10.
19. Michael TC, Veerappan AR, Shanmugam S. Effect of internal pressure and shape imperfections on plastic loads of pipe bends under in-plane closing moment. *Engineering Fracture Mechanics*. 2013;105:1-15.
20. Duan, Z. X., & Shi, K. (2013, November). Analysis and experiments on the plastic limit load of elbows under combined pressure and in-plane closing bending moment. In *Advanced Materials Research* (Vol. 774, pp. 1090-1097).

21. Simha CHM. Limit load solutions for cracked elbows subjected to internal pressure and in-plane bending. *Journal of Pressure Vessel Technology*. 2012;134(4):1-11.
22. Zhang, S. H., Zhao, D. W., & Gao, C. R. (2012, January). Limit analysis of defect-free pipe elbow under internal pressure with MY criterion. In *Applied Mechanics and Materials* (Vol. 127, pp. 79-84).
23. Chattopadhyay J, Kushwaha HS, Roos E. Improved integrity assessment equations of pipe bends. *International Journal of Pressure Vessels and Piping*. 2009;86(7):454-473.
24. Lee SM, Choi YH, Chung HD, Chang YS, Kim YJ. Plastic limit analysis of an elbow with various wall-thinning geometries. *In Key Engineering Materials*. 2008, December;385:833-836.
25. Vishnuvardhan S, Raghava G, Gandhi P, Goyal S, Gupta SK, Bhasin V. Ratcheting strain assessment in pressurised stainless steel elbows subjected to in-plane bending. *Procedia Engineering*. 2013 Jan 1;55:666-670.
26. Mechanical APDL and Mechanical Applications Theory Reference: Release 15.0 (2013). USA, SAS IP, Inc: ANSYS
27. Basquin OH. The exponential law of endurance tests. *In Proc Am Soc Test Mater*. 1910;10:625-630.

How to cite this article: Harun MF, Mohammad R, Kotousov A. Effect of wall thinning on deformation and failure of copper-nickel alloy elbows subjected to low cycle fatigue. *Mat Design Process Comm*. 2020;2:e111. https://doi.org/10.1002/mdp2.111

VIBGYOR ePress

International Journal of
Metallurgy and Metal Physics

Effect of Shot Size in Surface Improvement via Shot Peening; Analytical, Modeling and Experimental Approaches

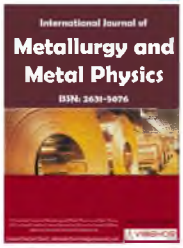

ISSN: 2631-5076

Y Prawoto[1], PG Mazein[1], AV Kosterin[1] and Z Ahmad[2]*

[1]*Department of Mechanical Engineering, South Ural State University, Russia*

[2]*Department of Mechanical Engineering, Universiti Teknologi Malaysia, Malaysia*

Abstract

This paper discusses about the surface engineering improvement by means of shot peening. Shot peening improves the surface engineering quality by eliminating the tool marks, such as machining, grinding, stamping and other surface defects. Most importantly, the improvements of shot peening are produced by combination of compressive stress and cold work. Compressive stresses are beneficial in increasing resistances to fatigue failures, while the cold work effects of shot peening treatments can increase the surface hardness. It employs a steel shot media running at high speed to smash the material's surfaces systematically, which results in a compressed and condensed surface. Several factors influence the effectiveness of shot peening. They are namely shot nature, shot size, shot hardness, Almen intensity, shot angle and coverage. The focus of this research is finding the influence of the shot size. The approaches used are analytical, computational, and experimental studies. The center of the study is the influence of shot size in the generation of the compressive residual stress. Through analytical, computational and experimental approaches, it is confirmed that the shot size has influence on the depth of the peak residual stress rather than the surface residual stress. This research reaffirms the qualitative understanding with quantitative and comprehensive approaches that can also be used for further in depth research in surface engineering improvement especially via shot peening.

Keywords

Shot peening, Shot size, Residual stress, Surface engineering, Cold work

Introduction

Shot peening has been used for decades as a measure to overcome surface engineering problems in various industries. Its improvements are produced mainly by combinations of compressive residual stress and cold work. Compressive residual stresses are known to be beneficial in increasing resistances to fatigue failures and corrosion fatigue, while the cold work effects of shot peening treatments can increase the surface hardness of many materials [1]. It is believed to be the most economical and effective method of producing and making surface residual compressive stresses to increase the product life of treated metal parts. The increased strength of treated parts allows for light-

***Corresponding author:** *Y Prawoto, Department of Mechanical Engineering, South Ural State University, 76, Lenin prospect, Chelyabinsk, 454080, Russia*

Accepted: June 24, 2019; **Published:** June 26, 2019

ISSN 2631-5076

Citation: Prawoto Y, Mazein PG, Kosterin AV, Ahmad Z (2019) Effect of Shot Size in Surface Improvement via Shot Peening; Analytical, Modeling and Experimental Approaches. Int J Metall Met Phys 4:033

er-weight parts that exhibit high wear and fatigue resistance.

The process can be defined as work hardening to the surface of components by propelling streams of spherical shots to the surface. The surface layer of material yields plastically to generate residual compressive stress. Among the practitioners, it has been known well that many parameters influence the efficiency of shot peening process. These are the peening coverage, saturation, shot material, shot size, speed, and peening time [2].

In this research, the focus is on the effect of the shot size. This topic is chosen due to the reason that fundamental understanding on this influence is low. For very long time, this subject has been regarded as a "black engineering" which the perceived of benefit using larger size is real but the reasons of those benefits were not disseminated by those who understand. In a way this paper is promoting to the academics for the science of shot peening, instead of keeping the "black art of shot peening" in the industry. This attempt is also on the line with the policy among the shot peeners [3] from long time ago.

Analytical Solution

The starting point for the construction of the shot peening model is the solution of the problem for a single impact of a ball on a half-space [4]. The initial data for the models are:

V - Speed of flying shot balls;

R - Radius of shot balls;

ρ - Density of the shot ball material;

E - Elastic modulus;

μ - Poisson's ratio;

$\sigma_u = G_u(\varepsilon_u)$ - Material hardening curve.

A ball flying at a speed V hits the surface, contact forces develop in the contact zone, and the kinetic energy of the ball begins to be transformed into the elastic energy of the ball/half space and plastic deformation of the material to be shot peened. After the velocity of the ball becomes zero, the following condition is achieved:

$$\frac{mv^2}{2} = K(A\Pi + A\text{Ш}) \quad (1)$$

Where

$A\Pi$ - Is half-space energy;

$A\text{Ш}$ - Elastic energy of a ball;

K - Correction factor, taking into account the influence of the roughness of the hydrodynamic film formed at the moment of impact.

Equation (1) is the starting point for the formation of boundary conditions for the contact problem with an inhomogeneous half-space. In order to calculate the work $A\Pi$, it is necessary to find the stress distribution in the half-space. To do this, we solve a system of differential equations describing the elastoplastic behavior of the material. Taking into account the axial symmetry, the set of equations is most conveniently written in the cylindrical coordinate system *(r,ϑ,Z),* where *r* - radius, *Z* - axis, directed along the axis of symmetry, *ϑ* - polar angle.

It is assumed that the mass forces are absent after collision, so the equations of equilibrium are as follows:

$$\frac{d\sigma_r}{dr} + \frac{d\tau_{rz}}{dZ} + \frac{\sigma_r - \sigma_\theta}{r} = 0 \quad (2a)$$

$$\frac{d\sigma_Z}{dZ} + \frac{d\tau_{zr}}{dr} + \frac{\tau_{zr}}{r} = 0 \quad (2b)$$

In what follows, the following notations are used:

σ_r, σ_Z - Radial and axial stresses;

ε_r, ε_Z - Radial and axial deformations;

u, ω - Radial and axial movements;

$\tau_{zr} = \tau$ - Tangential stresses;

$\gamma_{Zr} = \gamma$ - Shear strain;

θ - Bulk deformation.

For the convenience of solving the equation (2a, 2b), they are transformed into:

$$\frac{d(\sigma_r r)}{dr} + \frac{d(r\tau_{rz})}{dZ} + \sigma_\theta = 0; \quad (3a)$$

$$\frac{d(\sigma_Z r)}{dZ} + \frac{d(\tau_{zr} r)}{dr} = 0 \quad (3b)$$

This is done to make it easier to approximate the system being solved on the *Z* axis. Indeed, the system (3a,3b) can be correctly solved only under the condition that:

$$\lim_{r\to 0} r\sigma_r = 0, \lim_{r\to 0} r\sigma_Z = 0 \quad (4)$$

These limiting relations are also established when finite-difference formulas are realized. To solve the problem, the finite volume of the half-space

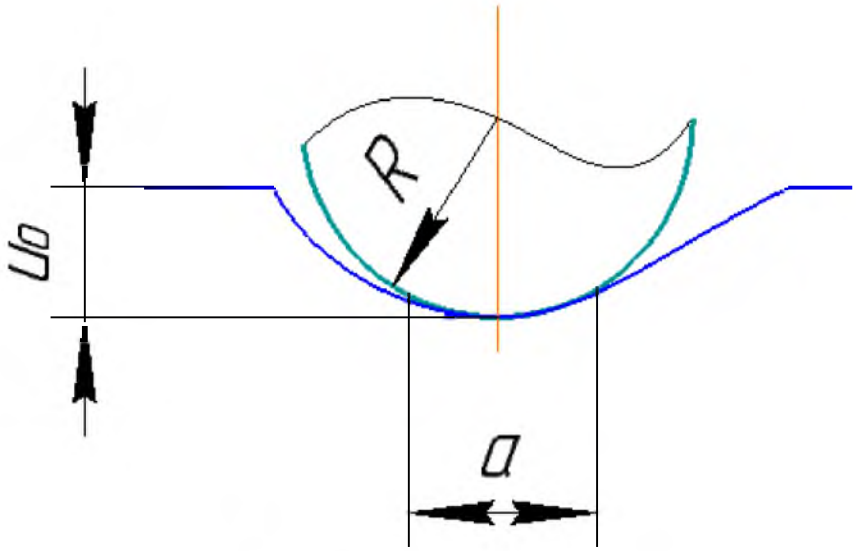

Figure 1: Diagram of contact area.

in the form of a cylinder of radius *R* and height *H* are selected. On the upper base of the cylinder, the boundary conditions are given in the displacements (Figure 1), which are: a) Within the contact area $u = u_0$, $\omega = \omega_0$, where (u_0, ω_0) is the introduction of an indenter into a half-space at specified distances from the Z axis; b) Outside the contact area it is free, that is, at the corresponding nodes the system (Equation 4) is solved.

In addition, in connection with the lack of friction, the tangential stresses on the surface are zero $\tau = 0$. On the lateral face of the cylinder $r = R$ and on the lower base $Z = H$ the boundary conditions are given in the stresses, which are calculated from the formulas of the theory of elasticity, namely, on the lateral surface:

$$\sigma_r = \sigma_r^{y\Pi p}(R,Z);\ \tau = \tau^{y\Pi p}(R,Z) \qquad (5a)$$

at the bottom:

$$\tau_r = \tau_r(r,H);\ \sigma_z = \sigma_z^{y\Pi p}(r,H), \qquad (5b)$$

Where $\sigma_r^{y\Pi p}, \sigma_z^{y\Pi p}, \tau^{y\Pi p}$ are calculated from the formulas for solving the problem of indentation by a spherical indenter into an elastic half-space. In this case, the dimensions of the cylinder must be chosen so that the area of plastic deformation is inside the cylinder. On the axis of symmetry $r = 0$ as boundary values we take the following conditions: $u_r = 0$, since on the axis of symmetry the radial displacement is zero; $\tau_{zr} = 0$ similarly, by virtue of symmetry.

To describe the plasticity processes, we use the equations of the theory of small elastoplastic deformations and the method of elastic solutions, which, after some transformations, can be written in the form of Hooke's law:

$$\varepsilon_r = \frac{1}{E^*}\left[\sigma_r - V^*(\sigma_\theta + \sigma_r)\right]; \qquad (6a)$$

$$\varepsilon_z = \frac{1}{E^*}\left[\sigma_\theta - V^*(\sigma_r + \sigma_z)\right]; \qquad (6b)$$

$$\varepsilon_\theta = 0,\ \gamma = \frac{1}{\sigma^*}\tau, \qquad (6c)$$

Where

$$E^* = \frac{\frac{\sigma_u}{\varepsilon_u}}{1 + \frac{3-2V}{3E}\cdot\frac{\sigma_u}{\varepsilon_u}};\ \sigma^* = \frac{\sigma_u}{3\varepsilon_u}; \qquad (7a)$$

$$V^* = \left(\frac{1}{2} - \frac{1-2V}{3E}\cdot\frac{\sigma_u}{\varepsilon_u}\right)\Big/\left(1 + \frac{1-2V}{3E}\cdot\frac{\sigma_u}{\varepsilon_u}\right), \qquad (7b)$$

Here σ_u - Stress intensity;

ε_u - Strain intensity.

Then the solution of the problem in the theory of plasticity is reduced into solving a problem of the contact theory of elasticity with variable elasticity parameters, determined by the formula described in Equations (6) and (7), and the relationship between the elasticity parameters:

$$\sigma^* = E^*/2(1+V^*) \qquad (8)$$

The solution of contact tasks is organized as follows:

-The initial introduction of the ball into the half-space is specified and, with the given boundary conditions, the method of variable elasticity parameters determines the stresses and deformations in the material; the energy of the deformed half-space is then determined from the formulas:

$$A = \int_0^H 2\pi \int_0^R rW dr dz, \quad (9)$$

Where W - Energy density.

$$W = W_o + W_\Phi, \quad (10)$$

Where W_o - Bulk deformation energy; and

W_Φ - Forming energy;

$$W_o = \frac{1-2V^*}{3E^*}\left(\sigma_r + \sigma_Z + \sigma_\theta\right)^2; \quad (11)$$

$$W_\Phi = \int_0^\varepsilon \sigma_u \, \varepsilon_u d\varepsilon_u \quad (12)$$

The verification of the fulfillment of the condition is by taking into account the assumption that the ball is perfectly rigid and $AIII$ = 0. If the condition does not hold, then we continue to insert the ball into the half-space, until the condition is met.

The method of variable elasticity parameters is as follows. In the first approximation, solve the usual problem of the theory of elasticity, when the variable elasticity parameters are constant $E^* = E$, $V^* = V$ since the system becomes ordinary Hooke's law. At the first stage, we use the analytical formulas. From the obtained value, we find the deformations $\varepsilon_z^{(1)}, \varepsilon_r^{(1)}, \varepsilon_\theta^{(1)}$ and the stresses $\sigma_z^{(1)}, \sigma_r^{(1)}, \sigma_\theta^{(1)}$. According to the last values, at each point we determine the stress intensity $\sigma_u^{(1)}$ and the strain intensity $\varepsilon_u^{(1)}$. From the deformation curve we find the stress intensity $\sigma_u^{(1)^*}$, which corresponds to the calculated value $\varepsilon_u^{(1)}$, then we set $\sigma_1^* = \sigma_u^{(1)^*} / 3\varepsilon_u^{(1)}$, and find the modules E_1^* И V_1^*, according to Equations (7a, 7b).

In the second step we solve the problem of the theory of elasticity with the obtained elasticity parameters, we determine in the second approximation the displacement $u^{(2)}$ and $\omega^{(2)}$, then $\varepsilon_Z^{(2)}, \varepsilon_r^{(2)}, \varepsilon_\theta^{(2)}$ И $\sigma_Z^{(2)}, \sigma_r^{(2)}, \sigma_\theta^{(2)}$, from them we find the intensities $\sigma_u^{(2)}$, $\varepsilon_u^{(2)}$ at each point of space, we calculate $\sigma_u^{(2)^*}$ by the deformation curve, we assume $\sigma_2^* = \sigma_u^{(2)^*} / 3\varepsilon_u^{(2)}$ etc.

The calculations are continued until the obtained results of the approximation calculations are different from the results (n - 1) of approximations by a given amount with the required accuracy. As the main criterion in the program, the condition, $\left|\sigma_n^* - \sigma_{n-1}^*\right| < \varepsilon$, which means virtually invariance of the elastic parameters, thus process converges.

The impact of a ball on a surface is a complex process, for the description of which it is necessary to use the equations of thermoelasticity, plasticity, impact theory, hydrodynamics. In addition, the presence of a complex surface profile, which is formed due to roughness, makes this task difficult to resolve. At the same time, as the analysis has shown, it is possible to identify the determining equations on which the behavior of the model depends and discard the remaining nonessential bonds. Since the speed of flying ball in the process of hydrobasting is not high, then we neglect the dynamic effects, and assume that the shock is quasistatic. It is quasistatic if:

- The deformations are considered to be concentrated in the vicinity of the contact area and are determined by the static theory, the wave motion in the bodies is neglected;
- Each body moves at any time with the velocity of its center of mass. The quasistatic conditions remain valid also in the case of plastic deformations, since the presence of plastic flow reduces the intensity of the contact pressure and, consequently, the energy going to the elastic wave motion. In the shot peening, the impact speed is known to be up to 70 m/s, it is possible to use the relations for inelastic contact stresses under static conditions with the yield stress is replaced by a dynamic yield strength. For this reason, we neglect the influence of thermal stresses, since even assuming that the entire energy of the ball is spent on heating, it still does not suffice to exert a significant influence on the distribution of residual stresses. In practice, we assume that the surface is perfectly smooth, and the expenditure of energy expended on the deformation of the scallops will be taken into account in formula (3a, 3b) by introducing corresponding corrections in the coefficient K.

Meanwhile, it is known from experiments and numerical calculations that the stress intensity is maximal on the axis of symmetry of the imprint and gradually decreases, tending to zero with increasing distance from the axis of symmetry of the print. With this in mind, for stress intensity, we can write the expression of:

$$\sigma_u = \beta(Z) \cdot e^{-\varepsilon r^2} \quad (13)$$

Applying similar arguments for residual stresses and taking into account that they essentially depend on the yield strength of the material, we obtain the expression:

$$\sigma_r^{\text{OCT}} = \theta_r(Z)(1-\mu_r r^2)/k_r\sigma_T; \quad (14a)$$

$$\sigma_\theta^{\text{OCT}} = \theta_\theta(Z)(1-\mu_\theta r^2)/k_\theta\sigma_T, \quad (14b)$$

Where σ_T - Yield strength;

k_r and k_θ - Co-efficients of sensitivity of residual stresses to the yield strength of the material.

The functions $\beta(Z), \theta_r(Z), \theta_\theta(Z)$ are arbitrary, but based on physical meaning it is necessary to demand that:

$$\lim_{r\to\infty} \beta(Z) = 0; \quad (15a)$$

$$\lim_{r\to\infty} \theta_r(Z) = 0; \quad (15b)$$

$$\lim_{r\to\infty} \theta_\theta(Z) = 0 \quad (15c)$$

Figure 2 schematically shows the distribution of intensity of load and residual stresses in the area of prints, which are calculated from formulas (13) and (14). These formulas reflect the qualitative picture of the distribution of residual stresses.

We expand the function (13) into the Taylor series.

$$\sigma_u = \beta(Z)\left[1 + \sum(-1)^2 \frac{1}{n!}\varepsilon^n r^{2n}\right] \quad (16)$$

If the yield stress is subject to the condition

$$\sigma_T \le \sigma_u^{\max}, \quad (17)$$

Then in Equation (16) we can drop all terms except the first with a small error, as a result we obtain:

$$\sigma_u = \beta(Z)\left[1 - \varepsilon r^2\right] \quad (18)$$

Using the expression in Equation (18) we find the current radius of the hardening area:

$$\overline{\sigma_T} = \beta(Z)\left[1 - \varepsilon l^2\right], \quad (19)$$

Hence

$$l^2 = \frac{1}{\varepsilon}\left(1 - \frac{\overline{\sigma_T}}{\beta(Z)}\right) \quad (20)$$

Now, taking into account Equation (18), we obtain:

$$F(Z,l) = \int_0^l \alpha\beta(Z) r(1-\varepsilon r^2)dr = \alpha\beta(Z)\, l^2\left(\frac{1}{2} - \frac{\varepsilon l^2}{4}\right), \quad (21)$$

While taking into account Equation (19):

$$F(Z,l) = \alpha\beta(Z)\frac{1}{4\varepsilon}\left(1-\frac{\overline{\sigma_T}}{\beta(Z)}\right)\left(1+\frac{\overline{\sigma_T}}{\beta(Z)}\right) \quad (22)$$

Further, we take the integrals for F_r and F_θ

$$F_r = 2\pi\int_0^R r\theta_r(Z)(1-\mu_r r^2)/k_r\overline{\sigma_T}(Z)dr \quad (23)$$

Obviously, in order to take this integral, it is necessary to specify the limits of integration. The radius of integration *R* will be found from the expression:

$$\theta_r(Z)(1-\mu_r r^2)/k_r\overline{\sigma_T} = 0, \quad (24)$$

Hence:

$$R = \sqrt{\frac{1}{\mu_r}} \quad (25)$$

Integrating (23) while taking into account (25), we obtain:

$$F_r(Z,l) = \frac{\theta_r(Z)}{4\mu_r k_r \overline{\sigma_T}(Z)} \quad (26)$$

Obviously, by carrying out similar actions for F_θ we obtain:

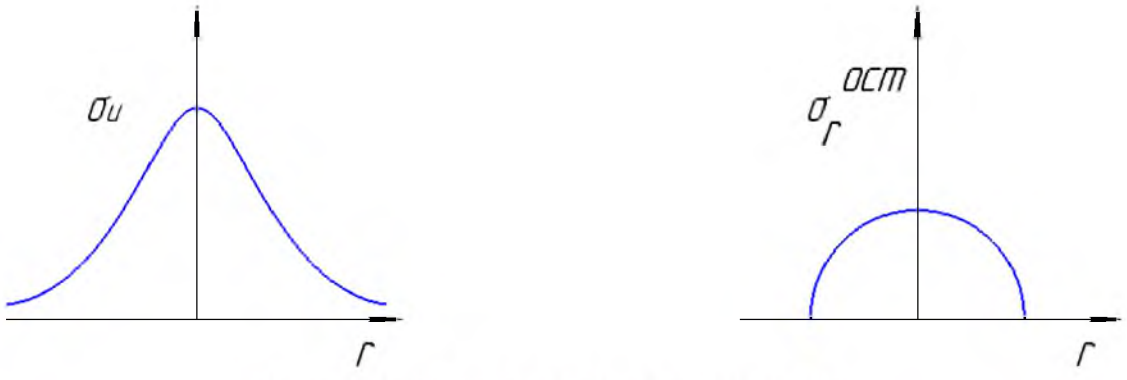

Figure 2: Stress distribution in the reference area.

$$F_\theta(Z,l) = \frac{\theta_\theta(Z)}{4\mu_\theta k_\theta \overline{\sigma_T}(Z)} \quad (27)$$

We now substitute the obtained expression in Equations (22), (26), (27) into Equation (3).

$$\frac{\overline{d\sigma_T^{\Sigma}(z,t)}}{dt} = 2\pi q\left[\alpha\beta(Z)\frac{1}{4\varepsilon}\left(1-\frac{\overline{\sigma_T^2}}{\beta^2(Z)}-\frac{1}{2\varepsilon}\left(1-\frac{\overline{\sigma_T}}{\beta(Z)}\right)\right)\right]; \quad (28a)$$

$$\frac{\overline{d\sigma_X^{\Sigma\ \text{ОСТ}}}}{dt} = \frac{2q}{\pi}\left[\frac{\theta_r(Z)}{4\mu_r k_r \overline{\sigma_T}} + \frac{\theta_\theta(Z)}{4\mu_\theta k_\theta \overline{\sigma_T}}\right] \quad (28b)$$

We now consider in more detail the first differential equation, since it does not depend on $\sigma_{(Z,t)}^{\Sigma\ \text{ОСТ}}$, then it can be solved separately. For the convenience of the solution, we introduce the following coefficients:

$$k = 2\pi q;\ a = \frac{k(r-\alpha)}{4\varepsilon\beta(Z)};\ b = \frac{k}{2\varepsilon};\ c = \frac{\alpha k\beta(Z)}{4\varepsilon} \quad (29)$$

Then the first Equation (28) is transformed as follows:

$$\frac{d\overline{\sigma_T}(z,l)}{dt} = a\overline{\sigma_T^2}(z,t) - b\overline{\sigma_T}(z,t) + c \quad (30)$$

We shall seek a solution of (30) in the form of:

$$\overline{\sigma_T} = y_1 + \frac{1}{y'} \quad (31)$$

Where y_1 - Particular solution.

We assume that y_1 is a certain value that does not depend on the parameter *t*.

$$y_1 = Y \quad (32)$$

Then substituting Equation (32) into Equation (31) we obtain:

$$aY^2 + bY + c = 0 \quad (33)$$

Solving this equation for *Y* we obtain two roots:

$$Y_{1,2} = \frac{\beta(Z)}{2-a}\left(1 \pm \sqrt{1-a(2-a)}\right) \quad (34)$$

Now (30) it can be reduced to a linear differential equation:

$$\frac{d\overline{y}}{dt} + (2aY - b)\overline{y} = -a \quad (35)$$

Substituting here (34) and taking into account (28), (29), we obtain the equation:

$$\frac{d\overline{y}}{dt} + \frac{k}{2\varepsilon}(A_0 - 1)\overline{y} + \frac{k(r-a)}{4\beta(Z)\varepsilon} = 0, \quad (36)$$

Where

$$A_0 = 1 \pm \sqrt{1-a(2-a)} \quad (37)$$

For simplicity, suppose that the material is ideally hardened, then $\alpha = 1$ and (37) is transformed as follows:

$$\frac{d\overline{y}}{dt} + \frac{k}{4\beta(Z)\varepsilon} = 0 \quad (38)$$

Integrating (38), we obtain the expression:

$$\overline{y} = -\left(\frac{kt}{4\beta(Z)\varepsilon} + c_1\right) \quad (39)$$

Then (31) takes the following form:

$$\sigma_T = \beta(Z) - \frac{1}{\frac{kt}{4\beta(Z)\varepsilon} + c_1} \quad (40)$$

The constant c_1 is found from the boundary condition:

$$\overline{\sigma_T}\Big|^{t=0} = \sigma_T^{\text{ИСХ}}; \quad (41a)$$

$$\sigma_T(Z,t) = \beta(Z) - \frac{1}{c_1}; \quad (41b)$$

Hence c_1 is found:

$$c_1 = \frac{1}{-\sigma_T^{\text{ИСХ}} + \beta(Z)} \quad (42)$$

Substituting (42) into (41), we obtain:

$$\sigma_T = \beta(Z) - \frac{1}{\frac{kt}{4\beta(Z)\varepsilon} + \frac{1}{\beta(Z)-\sigma_T^{\text{ИСХ}}}} \quad (43)$$

Study the solution obtained by us. If the hardening time increases, then: $\sigma_T(Z,t) \to \beta(Z)$ in the limit:

$$\lim_{t\to\infty}\sigma_T(Z,t) = \beta(Z) \quad (44)$$

Now consider the relationship between residual stresses and deflection of control plates Δf.

For simplicity, we take in (30) that $\mu_r = \mu_\theta, k_r = k_\theta$, then we obtain:

$$\frac{d\overline{\sigma_X^{\Sigma\ \text{ОСТ}}}(Z,t)}{dt} = \frac{2q}{\pi}\left(\frac{\theta_r(Z) - \theta_\theta(Z)}{4\mu k\sigma_T(Z,t)}\right) \quad (45)$$

We substitute into the equation (45):

$$d = \frac{2q}{\pi}\left(\frac{\theta_r(Z) - \theta_\theta(Z)}{4\mu k}\right), \quad (46)$$

Then the equation takes the form:

$$\frac{d\overline{\sigma_X^{\Sigma\ \text{ОСТ}}}(Z,t)}{dt} = \left(\frac{d}{\sigma_T(Z,t)}\right) \quad (47)$$

Equation (40) is reduced to the form:

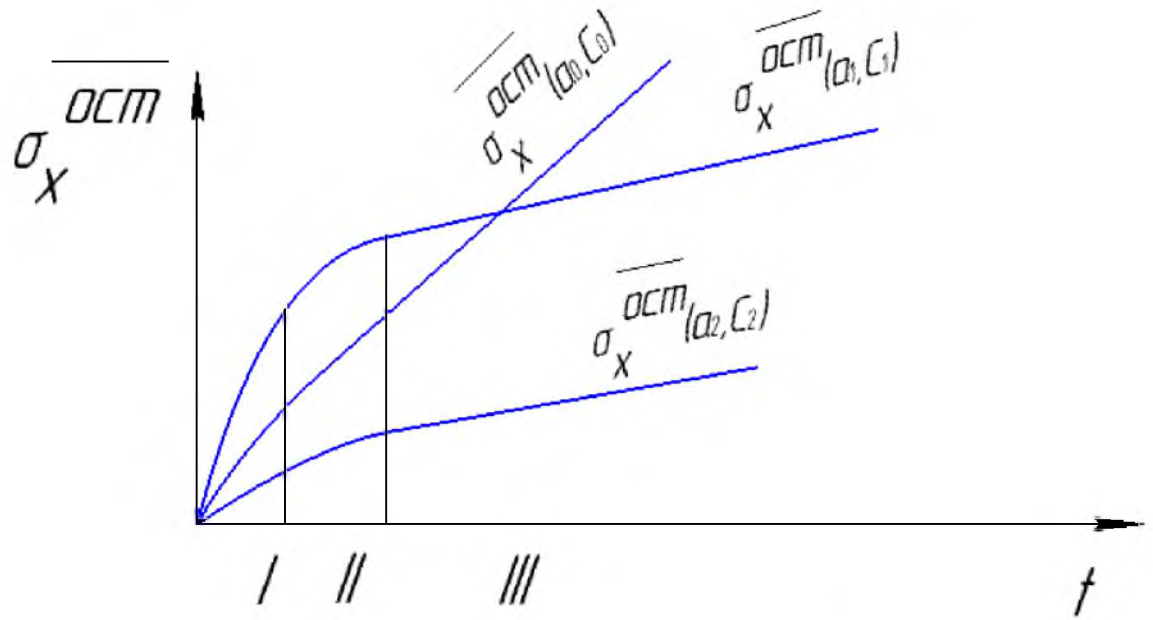

Figure 3: Dependence of residual stresses on hardening time.

$$\sigma_T = \frac{k\beta(Z)(\beta(Z)-\sigma_T^{ИСХ})t + 4\beta(Z)\varepsilon\sigma_T^{ИСХ}}{kt(\beta(Z)-\sigma_T^{ИСХ}) + 4\beta(Z)\varepsilon} \quad (48)$$

Taking into account (48), the equation (47) is becomes:

$$\frac{d\overline{\sigma_X^{\Sigma ОСТ}(Z,t)}}{dt} = \frac{d[kt(\beta(Z)-\sigma_T^{ИСХ}) + 4\beta(Z)\varepsilon]}{kt(\beta(Z)-\sigma_T^{ИСХ}) + 4\beta(Z)\sigma_T^{ИСХ}\varepsilon} \quad (49)$$

We make the substitution in the Equation (49):

$$a = k(\beta(Z) - \sigma_T^{ИСХ}); \; b = 4\beta(Z)\varepsilon; \quad (50a)$$

$$f = k(\beta(Z) \cdot (\beta(Z) - \sigma_T^{ИСХ}); \; g = 4\beta(Z)\sigma_T^{ИСХ}\varepsilon; \quad (50b)$$

$$\frac{d\overline{\sigma_X^{\Sigma ОСТ}}}{dt} = d\frac{at + b}{ft + g} \quad (50c)$$

We shall carry out a qualitative analysis of Equation (50). At the initial time, the increment of residual stresses should be maximal, since there is no hardening, in the future it should decrease to a certain limit, which can be easily found from the relation in Equation (50) (Figure 3).

$$\lim_{t\to\infty} \frac{d\sigma(Z,t)}{dt} = d\frac{a}{f} \quad (51)$$

The presence of this limit is easily explained by the existence of a maximum hardening limit:

$$\sigma_T < \sigma_T^{max}, \; 0 < t < \infty \quad (52)$$

This limit exists in many materials and is explained by its physical properties. We integrate now to equate to (50).

$$\overline{\sigma_X^{\Sigma ОСТ}} = d\left[\frac{at}{f} + \frac{fb - ag}{f^2}(\ln(ft + g) - \ln g)\right] \quad (53)$$

The analysis shows that the calculated curve can be divided into 3 phases:

I. Fast initial growth phase;

II. Transitional period;

III. Saturation phase.

Since the solution of the adaptability equations at each i-th step of the integration requires the solution of the one-shot problem, it is most advantageous to apply the interactive solution methods, since the resolution of the equations at each new step begins with the previous solution, which increases the computational speed. In particular, here we have chosen a two-layer integration scheme for solving the problem. The main decision points listed below.

1) Based on the preset depth of ball penetration, determine the contact radius:

$$B = \sqrt{R_{Ш} \cdot D_e}, \quad (54)$$

Where $R_{Ш}$- Ball radius;

D_e - Depth of implementation.

2) Determine the number of nodes N1 in the contact area and check whether it falls into the

required range, if not, the calculation is terminated. This is done to ensure that the number of grid nodes does not exceed the specified range, and, on the other hand, that the accuracy of the solution is sufficient.

3) Determine the coordinates of the grid nodes X (1), Y (1).

4) Determine the force of the ball pressing:

$$P = \frac{8\sigma_0 BD_e}{3(1-\nu)'} \quad (55)$$

Where σ_0 - Initial shear modulus.

By the given force P and the radius of the print B determine the elastic stresses according to:

$$\sigma_r^{\text{уПр}} = \sigma_r^{\text{уПр}}(r,Z);\ \sigma_Z^{\text{уПр}} = \sigma_Z^{\text{уПр}}(r,Z);\ \sigma_\theta^{\text{уПр}} = \sigma_\theta^{\text{уПр}}(r,Z); \quad (56)$$

5) On the basis of (55) find the boundary conditions:

On the axis $r = 0$ we obtain:

$$\sigma_r = \sigma_\theta = K\left[(1+V)(1-Z\,arctg\frac{1}{Z} - \frac{1}{2(1+Z^2)})\right]; \quad (57a)$$

$$\sigma_Z = K\frac{1}{1+Z^2};\ \tau = 0 \quad (57b)$$

On the surface $Z = 0$ we have $\tau = 0$

$$\sigma_r\Big|r \le b = K\left[\sqrt{1-r^2} + \frac{1-2\nu}{3r^2}\left(\left(1-r^2\right)^{3/2}-1\right)\right]; \quad (58a)$$

$$\sigma_\theta\Big|r \le b = K\left[\sqrt{1-r^2} + \frac{1-2\nu}{3r^2}\left(\left(1-r^2\right)^{3/2}-1\right)\right]; \quad (58b)$$

$$\Big|r \le b = K\sqrt{1-r}\ ; \quad (58c)$$

$$\sigma_\theta\Big|r > b = -\sigma_r, \qquad \sigma_Z\Big|r > b = 0 \quad (58d)$$

6) Find the boundary conditions on the lateral face:

$$F_{Gb}(b,Z) = \sigma_r^{\text{уПр}}(b,Z); \quad (59a)$$

$$F_{\tau b}(b,Z) = \tau^{\text{уПр}}(b,Z); \quad (59b)$$

$$F_{GN}(r,H) = \sigma_r^{\text{уПр}}(r,H); \quad (59c)$$

$$F_{\tau N}(r,H) = \tau^{\text{уПр}}(r,H), \quad (59d)$$

Where b, H - Height and width of the calculation area.

7) On the basis of (58), find the elastic displacements at the nodes.

8) To solve the interatomic problem, take the calculated elastic stresses as initial conditions, in addition, assume at the boundary that the boundary conditions correspond to the conditions found from the elastic solution (58) and (59).

Determine the intensity of stresses taking into account the residual stresses $\sigma_X^{\text{ОСТ}}$:

$$\sigma_u = \frac{1}{\sqrt{2}}\sqrt{(\sigma_r+\sigma_X^{\text{ОСТ}}-\sigma_Z)^2+(\sigma_\theta+\sigma_X^{\text{ОСТ}}-\sigma_Z)^2+6\tau^2} \quad (60)$$

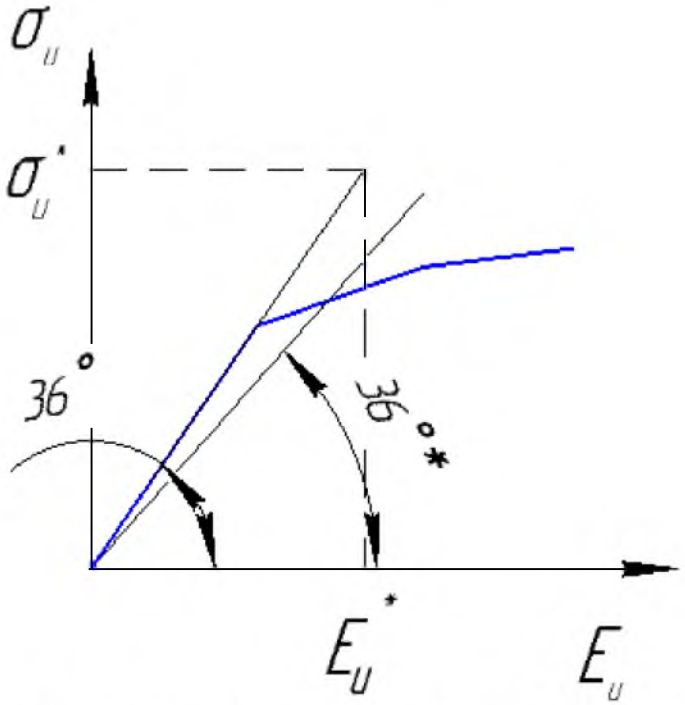

Figure 4: Diagram of the method of variable elasticity parameters.

To calculate the stress state in the plastic region, we use the variable elasticity method. According to this, the shear modulus σ and Poisson's ratio V at each point of the area are calculated (Figure 4). By σ^* and V^* their values depending on the value σ_u are indicated. σ and V are the values from the previous iteration. Find the intensity of the deformations by the formula:

$$\varepsilon_u = \frac{\sigma_u}{3}\left(\frac{1}{\sigma} + \frac{1-2V}{E}\right) \quad (61)$$

Further, we find the intensity along the deformation curve:

$$\sigma_u^* = a_n + b_n\varepsilon_u, \quad (62)$$

Where *n* - Number of the segment of the broken line, which approximates the curve, the deformation. After this, we determine the new value of the shear modulus by the formula.

$$\sigma^* = \frac{1}{\frac{3\varepsilon_u}{\sigma_u^*} + \frac{1-2v}{E}} \quad (63)$$

9) Find the deformations from the displacements, then calculate the stresses at the nodes from the obtained elastic deformations and the recalculated elastic modulus.

$$\sigma_r = \lambda\theta + 2\sigma\varepsilon_r; \quad (64a)$$

$$\sigma_\theta = \lambda\theta + 2\sigma\varepsilon_\theta; \quad (64b)$$

$$\sigma_Z = \lambda\theta + 2\sigma\varepsilon_Z; \quad (64c)$$

10) To determine the displacements at the grid nodes, it is necessary to compile a system of linear equations with fixed elastic parameters:

$$AY = F, \quad (65)$$

Where Y - Array of radial and axial displacements;

F - Boundary conditions, which are determined from the equations (59)

a) In order to find the matrix A, it is necessary to express the equilibrium equations in the form of a displacement function. Substituting (64) into the equilibrium equations, we obtain a system of second-order differential equations:

$$\Delta^2 u + \frac{1}{1-2V}\cdot\frac{d}{dx}\left(\frac{du}{dx} + \frac{dV}{dy} + \frac{dw}{dz}\right) + \frac{F_x}{\mu} = 0; \quad (66a)$$

$$\Delta^2 V + \frac{1}{1-2V}\cdot\frac{d}{dy}\left(\frac{du}{dx} + \frac{dV}{dy} + \frac{dw}{dz}\right) + \frac{F_y}{\mu} = 0; \quad (66b)$$

$$\Delta^2 w + \frac{1}{1-2V}\cdot\frac{d}{dz}\left(\frac{du}{dx} + \frac{dV}{dy} + \frac{dw}{dz}\right) + \frac{F_z}{\mu} = 0 \quad (66c)$$

The derivatives in (66) are found by three points:

$$y'(x_1) = \frac{1}{H}\left(-y_3 + 4y_2 - 3y_1\right); \quad (67a)$$

$$y'(x_i) = \frac{1}{H}\left(y_{i+1} - y_{i-1}\right),\ 1 < i < n; \quad (67b)$$

$$y'(x_n) = \frac{1}{H}\left(3y_n - 4y_{n-1} + y_{n-2}\right), \quad (67c)$$

Here $y_i = y(x_i)$, H - Double grid spacing.

Substituting the expression (67) into the equilibrium equation (66) and representing it as the product of matrices (65), we define the matrix A.

b) To solve the equation (65), we use the three-layer iterative method. According to this method, it is necessary to calculate the remainder by the formula:

$$r_k = AY_k - F \quad (68)$$

Calculate the vector column. A_{rk} for this we use the equations (65) and (66), but instead of displacement we substitute the remainder.

Calculate the coefficients A, E, F and if $K > 1$, then calculate the coefficients B, C, D:

$$A = (A_{rk}, r_k);\ B = (A_{rk}, r_{k-1}); \quad (69a)$$

$$C = (r_k, r_k - r_{k-1});\ D = (r_{k-1}, r_k - r_{k-1}); \quad (69b)$$

$$E = (A_{rk}, A_{rk});\ F = (r_k, r_k);\ F_{st} = (r_{k-1}, r_{k-1}) \quad (69c)$$

c) Calculate the new vector of the solution Y at the -th integration by the formulas:

$$Y^{(1)} = Y^{(0)} - \tau \cdot r_0, \text{ ПрИ } k = 1 \quad (70a)$$

$$Y^{(k+1)} = Y^{(k-1)} + \alpha\left(Y^{(k)} - Y^{(k-1)}\right) - \alpha\tau r_k, \text{ ПрИ } k \geq 2, \quad (70b)$$

Where

$$\alpha_k = \frac{(A-B)B - DE}{(C-D)E - (A-B)^2};\ \alpha_1 = 1; \quad (71a)$$

$$\tau_1 = \frac{A}{E};\ \tau_k = \frac{B}{E\alpha_k} + \frac{(A-B)}{E},\ k \geq 2 \quad (71b)$$

Since the contact task is being solved, it is necessary to fix the movement of the nodes in the contact area. In order for their values to remain unchanged in the iteration process, the discrepancy in these nodes is forcibly equated to zero, which leads to automatic fixation of displacements in these nodes.

The iterative process proceeds until the residual is sufficiently small, namely:

$$\left|\frac{F}{F_{st}} - 1\right| < \varepsilon, \quad (72a)$$

Where $\mathcal{E}$ - Relative accuracy.

Calculate the new elastic modulus from formulas (61), (62), (63). Find the change in the elastic modulus at the $(k + 1)$ iteration.

Further we check the condition: $\Delta E < \Delta E_g$, where ΔE - Maximum increment of the shear modulus; ΔE_g - Maximum increment error.

If the condition is not fulfilled, go to (10) and repeat the calculation again, otherwise go to the next step. This cycle limits the solution of the elastoplastic problem for a given depth of ball penetration.

Calculate the energy $э$ of the half-space;

$$э = \int_V (э_o + э_\Phi) dxdydz; \quad (73a)$$

$$э_o = \frac{1-2V^*}{6E^*}(\sigma_r + \sigma_\theta + \sigma_z)^2; \quad (73b)$$

$$э_\Phi = \frac{\sigma_u \varepsilon_u}{2}, \quad (73c)$$

Where $э_o$ - Bulk strain energy;

$э_\Phi$ - Forming energy.

Check whether the kinetic energy of the ball A_o is equal to the energy of the half-space. If not, go to step 17, otherwise go to the next step.

Define a new depth of the introduction of balls into a half-space, while:

$$h = h + \Delta h, \; if \; э < A_o; \quad (74a)$$

$$h = h - \Delta h, \; if \; э > A_o, \quad (74b)$$

Where h - Penetration depth of the ball;

Δh - Increment of penetration depth.

To achieve the convergence, the step is calculated using the following the formula:

if $э(h + \Delta h) > A_o$ and $э(h) < A_o$, then

$$\Delta h = \Delta h/2 \quad (75)$$

After recalculating the depth of implementation, go to step 1 of the algorithm.

11) Calculate the residual stresses by the formula:

$$\sigma_{ij}^{ост} = \sigma_{ij}^{H} - \sigma_{ij}^{y\Pi p}, \quad (76)$$

Where σ_{ij}^{H} - Load stresses;

$\sigma_{ij}^{y\Pi p}$ - Stresses, discharges, obtained from the elastic solution.

The solutions obtained from the algorithm are

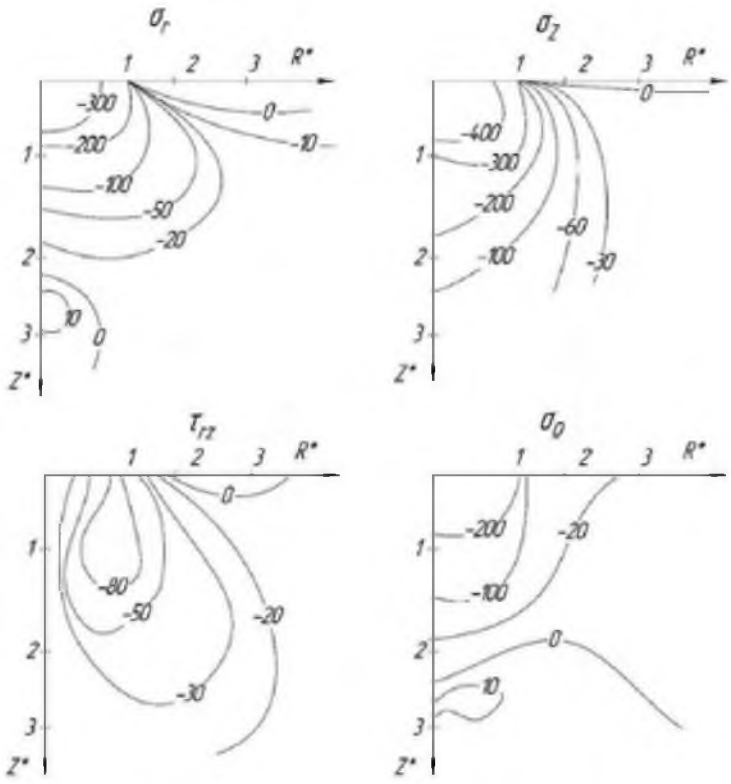

Figure 5: Results of calculation of stresses for a single print.

based on the fact that at a sufficiently large distance from the contact zone the elastoplastic solution converges to the elastic solution. This assumption allows to limit the calculated area to a cylinder of the radius B and the height H, and at the nodes located on the outer boundary of the cylinder, the displacements obtained from the elastic solution.

Figure 5 shows the distribution of stresses with $K_{ПроП} = 1$, the ball radius $R_{Ш} = 1,25\ mm$. The figure shows the example of the residual stress distribution with a dummy mechanical property of the steel materials. For our experiment, the comparable stress would be the right bottom stress distribution.

Finite Element Modeling

All computer modeling in the present study was conducted using the nonlinear finite element (FE) code LS-DYNA 971. A model of the workpiece surfaces was developed using a constant stress solid element formulation which suitably model the impacted surface response of the workpiece. The impacting balls of two different sizes namely 0.8 mm and 1.3 mm were also modelled using solid elements with reduced integration techniques in combination with hourglass control. In a way it is similar to that of Purohit's [5] with multiple shot balls. The workpiece is modelled with four geometrical parts with same nodes between the internal surfaces. The model was discretised using solid element with two mesh sizes to capture better simulation results. Stiffness-based hourglass control was employed to avoid spurious zero energy deformation modes and the use of reduced integration was to avoid volumetric locking. The elastic and elasto-plastic material models were used to model the impacting ball and the impacted surfaces, respectively. The material properties included for the impacted surface are the yield stress of 1433 MPa with a plastic hardening behavior. For the impacting ball, a very high value of stiffness has been assigned to represent high rigidity of the structure when contacting with other surfaces. The finite element discretization of the shot peening simulation is depicted in Figure 6. Shot peening loading was simulated by defining an impact velocity of 90 m/s to the impacting balls over a three repeated

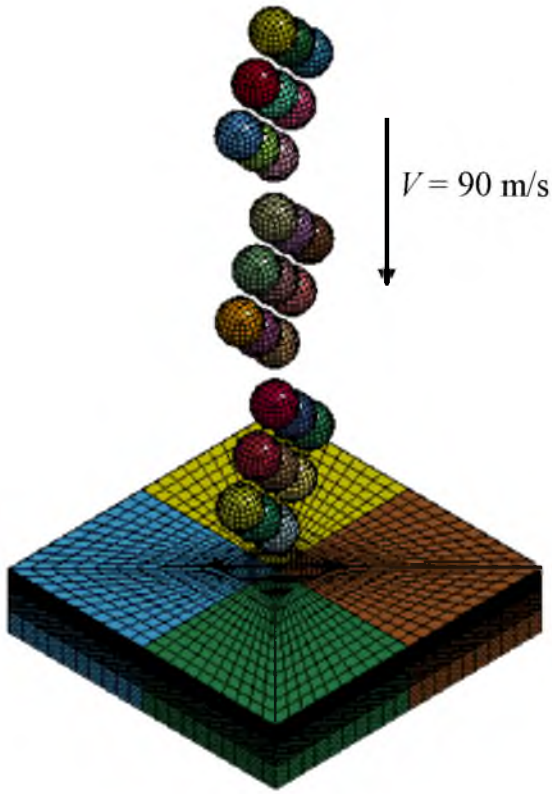

Figure 6: Finite element model of shot peening simulation under several impact sequences.

Impact point	x	y
1	0	0
2	D/2	0
3	D	0
4	0	D/2
5	D/2	D/2
6	D	D/2
7	0	D
8	D/2	D
9	D	D

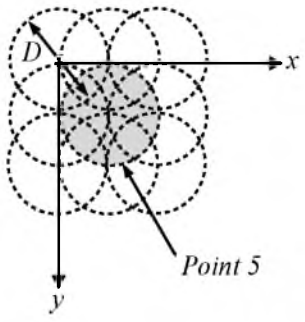

Figure 7: Schematic diagram of the impacting points and sequence on the workpiece model.

impact loading. Figure 7 shows the schematic diagram of the impacting points and sequence on the workpiece model. The evaluation of residual stress and impacting depth was carried out underneath of Point 5. The simulation was done in two separate phases namely explicit and implicit simulations. Explicate simulation was employed to simulate the impact loading on the workpiece. From this simulation, impact analysis may be carried out resulting in obtaining the initial stress field in the workpiece. Subsequently, the output obtained from explicit simulation was employed to simulate implicit simulation. Thereafter, the residual stress in material can be obtained from the implicit analysis on work piece stress after impact. The impacting ball was constrained to translate vertically only along the *z* axis, and the bottom and edges nodes of the workpiece surfaces were fully constrained as shown in Figure 7. A reliable contact modeling for the interaction between the impacting ball and workpiece is paramount and needs to be accurately established. Automatic surface to surface contact was defined for the contact interfaces of the impacting ball with the workpiece in order to avoid any penetration occurred. The friction coefficients associated with contact between the balls and workpiece were defined as 0.3 and 0.2 for the static and dynamic respectively.

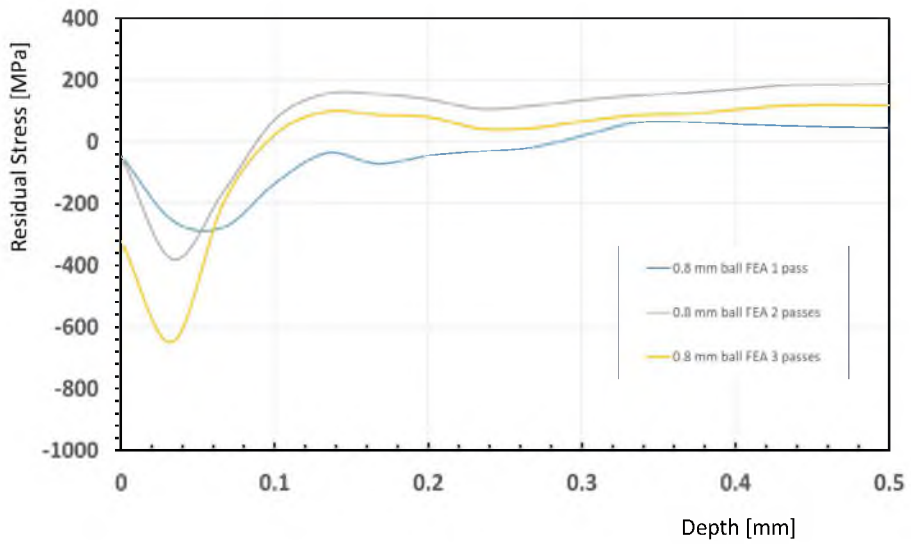

Figure 8: Residual stress computed with finite element model with the ball diameter of 0.8 mm.

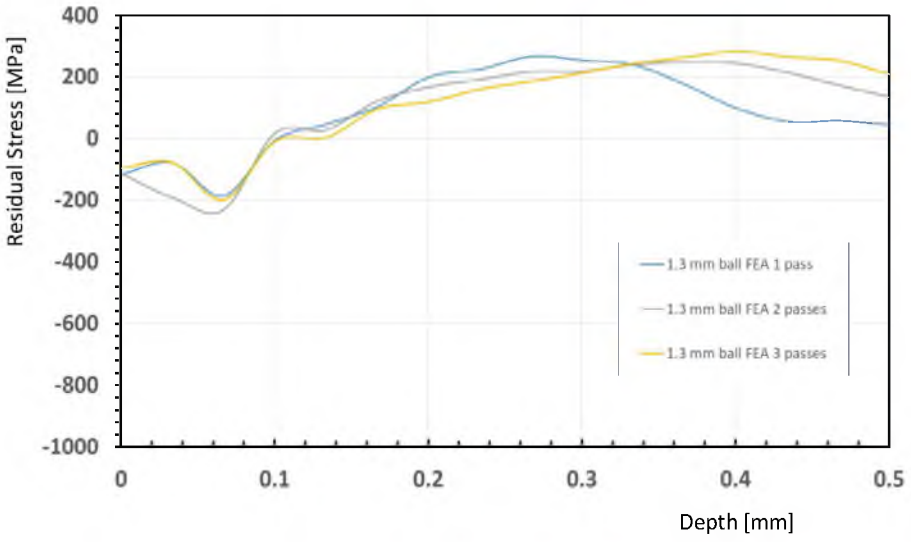

Figure 9: Residual stress computed with finite element model with the ball diameter of 1.3 mm.

Citation: Prawoto Y, Mazein PG, Kosterin AV, Ahmad Z (2019) Effect of Shot Size in Surface Improvement via Shot Peening; Analytical, Modeling and Experimental Approaches. Int J Metall Met Phys 4:033

Figure 8 and Figure 9 show the result of the FE models. One can see that as the number of the pass increases, the maximum compressive residual stress also increases. At the same time, the depth of the peak also increases as the size of the ball increases. These were in agreement with both our analysis and experiment.

Experiment

The experiment was done by shot peening on two different plates, namely plate A and plate B. On the plate A, shot ball size was 0.8 mm and on plate B, the shot ball size 1.3 mm. The experiment was performed with the same machine with the parameters to match the analysis. The coverage of the shot peening was approximately 98%. This is to mimic what is usually called saturated shot peening. Beyond this coverage, more shot peening amount that is put into the system will not affect the residual stress significantly. The samples were than profiled with an x-ray diffraction device. Figure 10 and Figure 11 show the results. The 0.8 mm ball produces slightly less than 300 MPa at the surface, while the 1.3 mm ball produces more than 500 MPa. The peak for the shot ball size of 0.8 mm produces 0.1 mm maximum depth of compressive residual stress, while the 1.3 mm ball produces peak at 0.19 mm. This trend is similar with both the analytical and finite element results as well as the finding of other researchers [6].

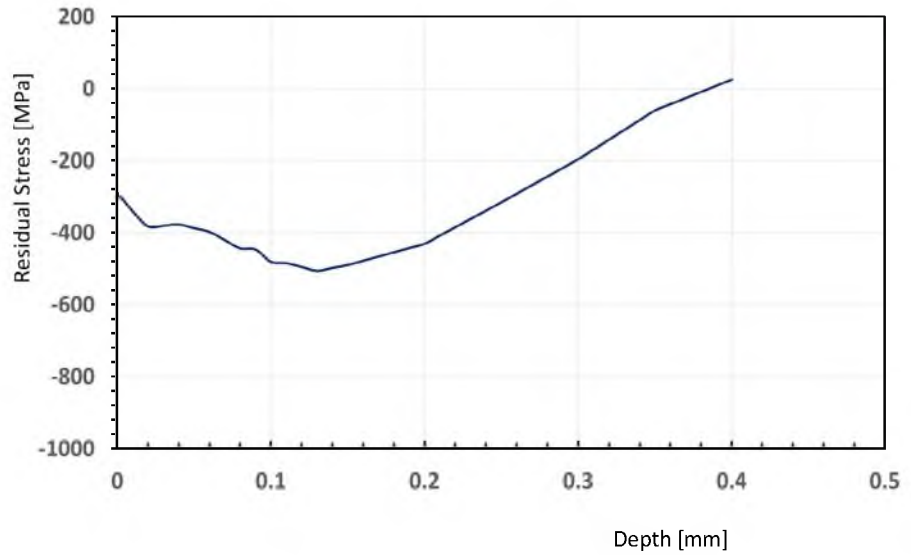

Figure 10: Results of experiment using 0.8 mm shot size.

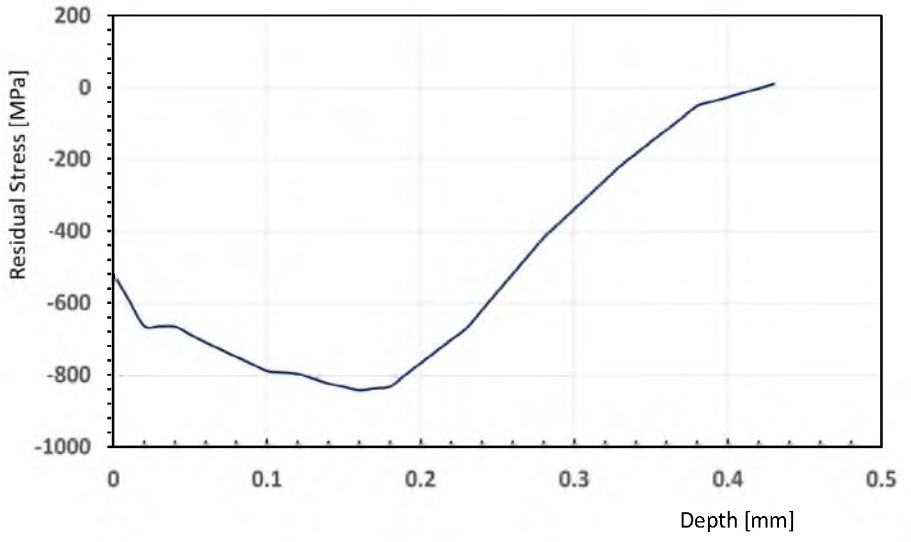

Figure 11: Results of experiment using 1.3 mm shot size.

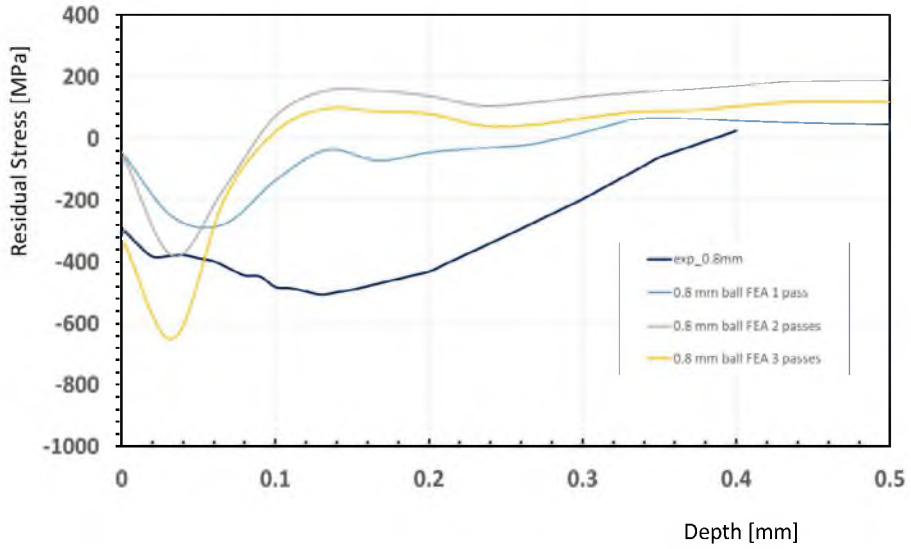

Figure 12: Comparison of FE modeling and experiment for shot ball size of 0.8 mm.

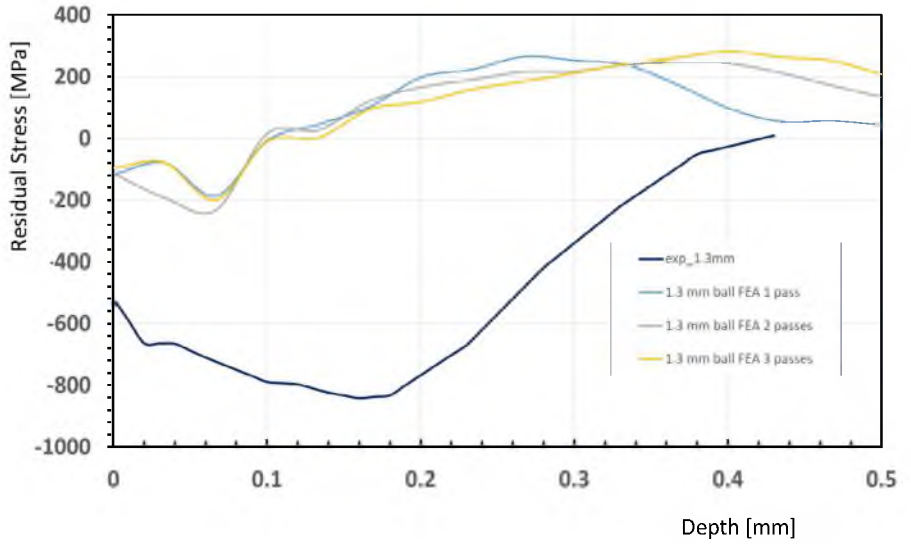

Figure 13: Comparison of FE modeling and experiment for shot ball size of 1.3 mm.

Discussions

Figure 12 and Figure 13 are the direct comparison between the simulation and the experiment. One can see that while the direct comparison do not match in detail, but they are at the right tendency. The disagreement between the analysis, finite element model and the experiment was expected from the beginning. The computation limitation was also prevented us to do until saturation, in our case, 3 passes. However, since this is our first attempt to academically materialize the concept of the shot peening in calculation such discrepancy is highly anticipated. Other researchers also pursue similarly [2,7-9]. Among the practitioners, the saturated residual stress at the surface is usually predicted as:

$$\text{Surface } \sigma_{RS}[\text{MPa}] = -276\frac{Ah}{R} + 7.1\,\gamma_R - 0.59\sigma_{pre} - 451 \quad (76)$$

At the surface, where Ah is the arc height and R is the radius of shot, while γ_R is the retain austenite. For the peak, usually it becomes

$$\text{Max. } \sigma_{RS}[\text{MPa}] = -172\frac{Ah}{R} + 7.1\,\gamma_R - 0.54\sigma_{pre} - 882 \quad (77)$$

The unit is in MPa. The above empirical equations are quite famous in the industrial world although it is lack of scientific basis. Based on Equations (76) and (77), and our measurement that arc-height are 0.54 and 0.28 respectively, our prediction of sur-

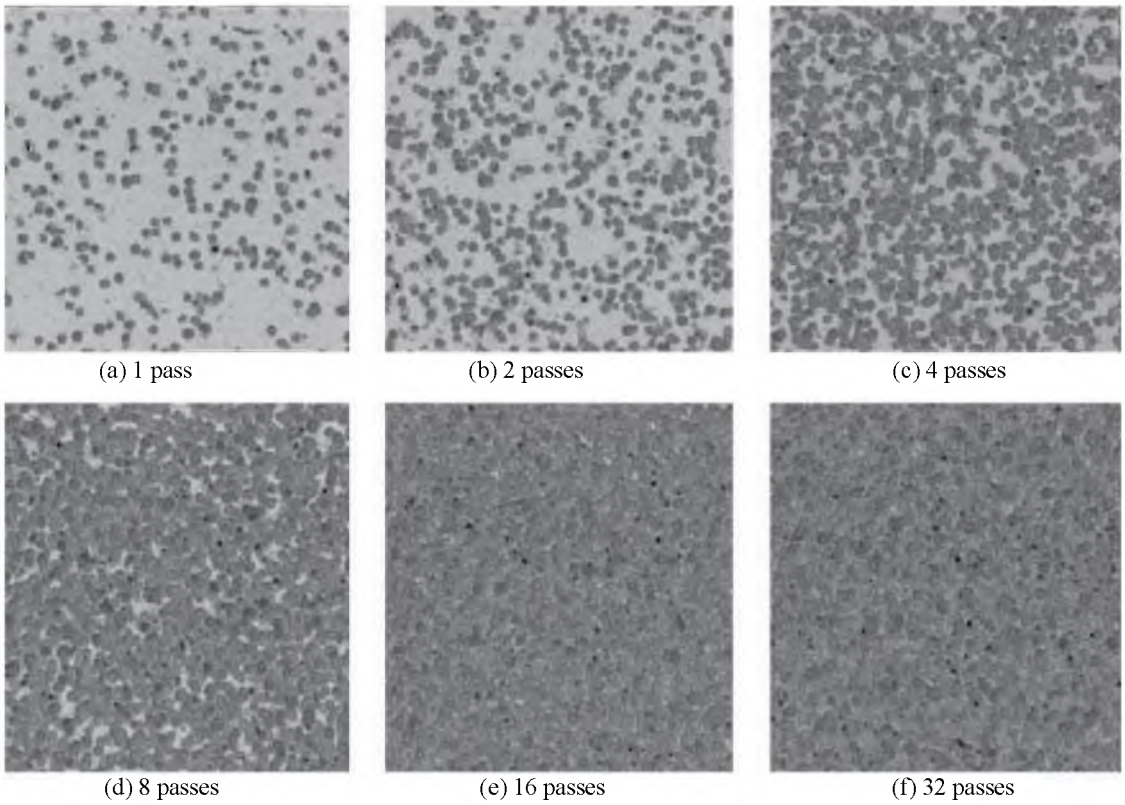

Figure 14: Shot peening coverage at different shot peening passes.

face residual stress would be -530 MPa and -512 MPa respectively. The peak residual stress would be 917 MPa and 906 MPa. Again, direct comparison of the prediction using these empirical equations with experiment and with computational results are still difficult. We can only say that the trend is similar.

Figure 14 shows the coverages at different passes. It shows clearly that our first attempt in this computation is still an early stage and can be modified into broader area and more variation of the coverage.

In the fatigue based industrial application, it is very critical that a product has both sufficient surface residual stress and depth of peak to prolong the fatigue life. This trend explain why some products use double shot peenings, which are the first using large shot ball and followed by smaller shot ball. This is thought to guaranty delaying both the fatigue crack initiation and early stage of fatigue crack propagation.

Conclusions

Through analysis, finite element modeling and experiment, it is proved that shot ball size influences mainly on the depth of the peak residual stress. This conclusion is nothing new among the practitioners. However, this research proved that academically this field has so much promise and potential to develop further. It would be an interesting topics to incorporate the chaos theory, since while the number of individual impacts is linearly proportional to shot flow, exposure area, and exposure time, the shot peening coverage is not linearly proportional because of the random nature of the process.

Acknowledgment

Part of the work was performed during the first author's stay as a visiting professor at the South Ural State University, Russia. The financial support and contribution from the International office of South Ural State University is highly appreciated.

References

1. Dounde AA, Seemikeri CY, Tanpure PR (2015) Study of shot peening process and their effect on surface properties : A review. IJEBEA 12: 104-107.
2. Higounenc O (2005) Correlation of shot peening parameters to surface characteristic. Icsp9 Shot Peen 28-35.
3. (1958) Shot Peening - Designer's guide to the process,

its applications. Mach Des 77: 116-125.

4. Miftahov AA, Mazein PG (2006) Modelling of residual stresses at shot peening.
5. Purohit R, Verma CS, Rana RS, Dwivedi R, Dwivedi S, et al. (2017) Optimization of process parameters of shot peening using ABQUS. Mater Today Proc 4: 2119-2128.
6. Gariépy A, Miao HY, Lévesque M (2017) Simulation of the shot peening process with variable shot diameters and impacting velocities. Adv Eng Softw 114: 121-133.
7. Bianchetti C, Delbergue D, Bocher P, Lévesque M, Brochu M (2019) Analytical fatigue life prediction of shot peened AA 7050-T7451. Int J Fatigue 118: 271-281.
8. Chang SH, Lee SC, Tang TP (2008) Effect of shot peening treatment on forging die life. Mater Trans 49: 619-623.
9. Dianyin HU, Ye Gao, Meng F, Song J, Wang Y, et al. (2017) A unifying approach in simulating the shot peening process using a 3D random representative volume finite element model. Chinese J Aeronaut 30: 1592-1602.

ISSN 2631-5076

Citation: Prawoto Y, Mazein PG, Kosterin AV, Ahmad Z (2019) Effect of Shot Size in Surface Improvement via Shot Peening; Analytical, Modeling and Experimental Approaches. Int J Metall Met Phys 4:033